ChemComm

FEATURE ARTICLE

View Article Online
View Journal | View Issue

Cite this: *Chem. Commun.*, 2022, **58**, 4005

Tailored porous framework materials for advancing lithium–sulfur batteries

Bingqian Liu [a] and V. Sara Thoi *[ab]

Received 16th December 2021,
Accepted 1st March 2022

DOI: 10.1039/d1cc07087h

rsc.li/chemcomm

Despite great promise as next-generation high-capacity energy storage devices, lithium–sulfur batteries still face technical challenges in long-term cyclability. With their porous structures and facile synthesis, metal–organic frameworks (MOFs) are tunable platforms for understanding polysulfide redox and can serve as effective sulfur hosts for lithium–sulfur batteries. This feature article describes our design strategies to tailor MOF properties such as polysulfide affinity, ionic conductivity, and porosity for promoting active material utilization and charge transport efficiency. We also present engineering approaches for implementing MOF-based sulfur cathodes for lithium–sulfur batteries with high volumetric density and under low temperature operation. Our studies provide fundamental insights into sulfur–host interactions and polysulfide electrochemistry in the presence of porous matrices, inspiring future designs of advanced batteries.

1. Introduction

The increasing global energy demand and climate change from fossil fuel consumption necessitate the implementation of renewable energy technologies. However, the intermittency of wind and solar power requires reliable energy storage. While secondary batteries are attractive storage devices due to their modularity and portability, current battery technologies, such as Li-ion batteries (LIBs), have yet to achieve the energy density and low cost for enabling widespread electrification. Among the various battery chemistries studied to date, lithium–sulfur (Li–S) batteries stand out as a promising alternative to LIBs. Lithium–sulfur batteries can achieve a high theoretical gravimetric energy density of 2572 W h kg^{-1}, nearly an order of magnitude higher than current LIBs. The abundance and low cost of sulfur also make Li–S batteries more affordable and environmentally benign than the incumbent Co-based LIBs. However, Li–S batteries suffer from poor cyclability due to a well-known phenomenon called the "shuttle effect".[1–4] During the discharge, cathodes undergo multi-electron conversion process, in which elemental sulfur is reduced to soluble Li_2S_x (x = 4–8) before terminating at insoluble Li_2S. The generated soluble polysulfides can leach from the cathode to the electrolyte, causing active material loss and electrode surface passivation. This shuttle effect leads to rapid capacity decay, high self-discharge rate, and high cell impedance.

One solution to mitigate polysulfide leaching is the adoption of sulfur host materials at the cathode. To achieve optimized active material utilization and cyclability, the polarity, porosity, and conductivity of the sulfur hosts should be considered as these properties are intimately linked with their ability to confine polysulfides and mobilize charge. Previous studies have utilized porous carbon materials,[5–8] metal oxides,[9–11] and polymers[12,13] as cathode additives. In comparison, metal–organic frameworks (MOFs) offer immense structural and chemical tunability for enabling polysulfide confinement *via* both physical encapsulation and chemical adsorption. The synthetic control over MOF properties such as particle morphology, porosity, and conductivity provides additional tailorability.[14–16] Furthermore, their porous nature permits host–guest interactions for polysulfide encapsulation and pathways for ion diffusion. To this end, MOFs with various compositions and pore structures have been used in Li–S cathodes to mitigate polysulfide dissolution.[17–21]

Our group has developed functionalization strategies aimed at enhancing polysulfide confinement and charge conduction. In particular, we have focused on a family of Zr-based MOFs as sulfur hosts due to their extraordinary electrochemical stability and structural versatility.[22] The hexanuclear Zr-oxo cluster enables different node connectivity by tuning quantity and geometry of the carboxylate linker.[23] In addition, missing linker defects can be introduced to Zr-MOFs, forming defect sites that can be functionalized post-synthetically.[24] Harnessing their facile functionality and robust host–guest chemistry, we have incorporated functional groups and redox-active components to facilitate polysulfide binding and charge transport (Scheme 1). Herein, we will detail our approach for designing advanced sulfur hosts and describe fundamental insights on MOF-sulfur interactions and polysulfide redox.

[a] *Department of Chemistry, Johns Hopkins University, 3400 N. Charles St., Baltimore, MD 21218, USA. E-mail: sarathoi@jhu.edu*
[b] *Department of Materials Science and Engineering, Johns Hopkins University, 3400 N. Charles St., Baltimore, MD 21218, USA*

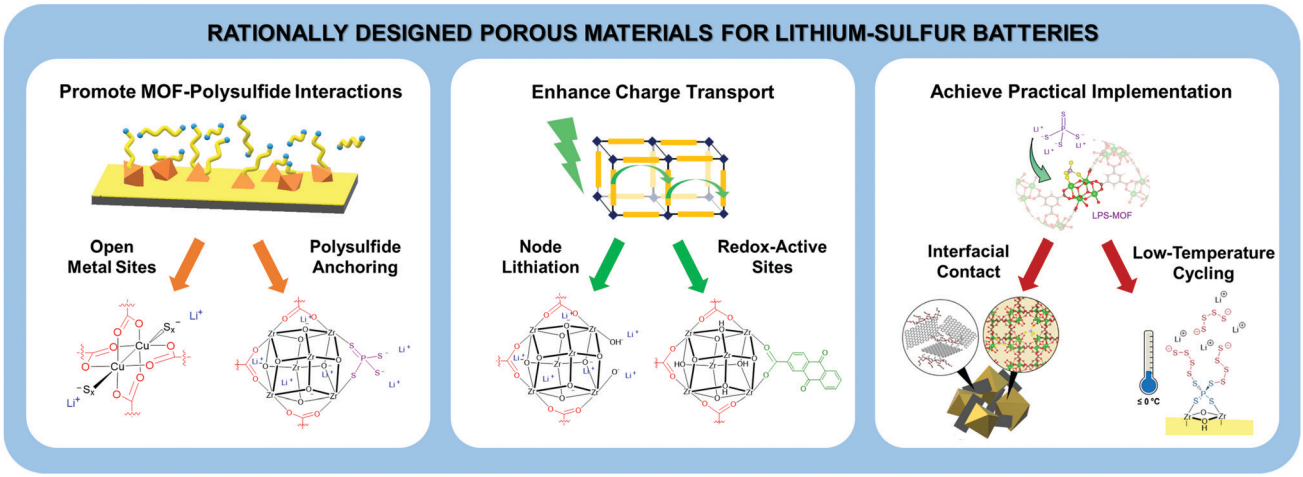

Scheme 1 Synthetic and materials engineering strategies employed for enhancing Li–S battery cycling performance.

2. Design strategies for constructing better sulfur cathodes

Motivated by previous studies on MOF hosts in Li–S batteries,[25–27] we devised new ways to increase polysulfide affinity, ionic conductivity, and charge transport efficiency in MOFs by taking advantage of their facile tunability and highly porous structure. With the incorporation of polysulfide anchoring groups and redox-active species, we demonstrated enhanced capacity retention and rate capability. Through the detailed analysis on polysulfide-MOF interactions and polysulfide redox in the presence of MOF matrices, we provided new chemical understanding and rational design strategies for porous materials with improved electrochemical performance.

2.1. Promoting interactions between MOFs and lithium polysulfides

Due to their highly porous nature, MOFs are suitable candidates for studying host–guest interactions. The versatility of pore geometries and volumes provides opportunities for optimizing ion diffusion. Other than physical encapsulation of polysulfides, the easily accessible defect sites in MOFs offer great potentials for chemically binding polysulfides. Herein, we design efficient sulfur hosts by tuning physical and chemical properties of MOFs.

2.1.1. Coordinatively unsaturated metal sites for polysulfide binding. Frameworks with open metal sites have high affinity for polysulfides.[28–30] Among them, CuBTC is a well-known MOF consisting of copper paddlewheel node and benzene-1,3,5-tricarboxylate (BTC) linkers. Upon thermal treatment, the axial aqua ligand bound to the copper node can be removed, resulting in coordinatively unsaturated copper sites. Previous studies show that multiple sulfur species are able to bind at these Lewis acidic Cu centers.[20,25,31] Our group took advantage of this property and employed CuBTC as a matrix for mitigating the shuttle effect. We thus constructed sulfur-loaded CuBTC composite cathodes and examined the Cu–S binding and their electrochemical performance (Fig. 1a).[32]

We first used computational and spectroscopic experiments to understand MOF-sulfur interactions in CuBTC. Density functional theory (DFT) calculations showed that sulfur clusters with different lengths (S_n, n = 2–8) favorably bind at the activated copper paddlewheel node. X-ray absorption spectroscopy (XAS) of sulfur-infused CuBTC (CuBTC@S) further confirmed sulfur coordination at the metal center. While X-ray absorption near-edge structure (XANES, Fig. 1b) spectra indicate the oxidation state of Cu remains +2 in CuBTC and CuBTC@S, a decreased white line intensity of CuBTC@S as a function of S:MOF ratio suggests reduced electron occupancy in the 3d states originating from Cu–S interactions. Extended

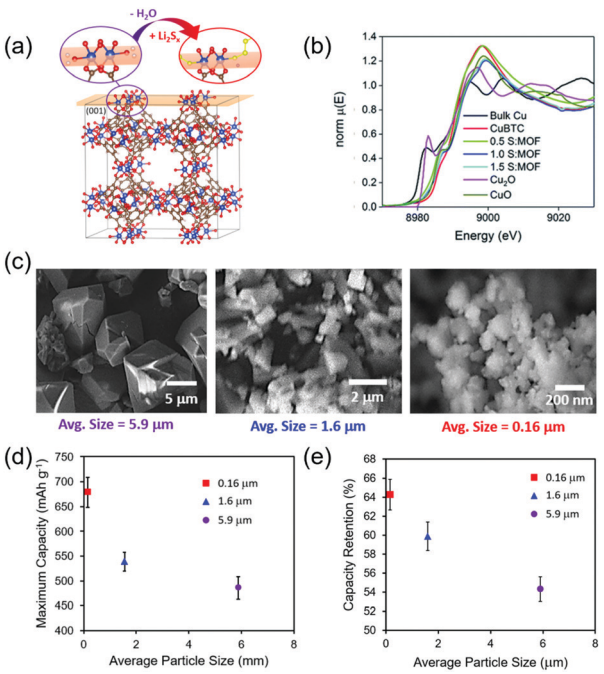

Fig. 1 (a) Solid-state structure of CuBTC and proposed polysulfide binding at surface Cu sites, (b) XANES profiles, (c) scanning electron micrographs showing CuBTC of different particle sizes, (d) average maximum capacity and (e) capacity retention (after 20 cycles) of CuBTC@S cells as a function of particle size. Reproduced from ref. 32 with permission from the Royal Society of Chemistry.

X-ray absorption fine structure (EXAFs) data also showed a decrease in Cu–O_{BTC} coordination number (CN) compared to pristine CuBTC, suggesting the presence of undercoordinated sites. The similar Cu–Cu CN indicates the Cu paddlewheel is structurally maintained upon sulfur infusion. Raman spectroscopy showed a blue shift of the Cu–Cu band and a red shift of Cu-ligand band, confirming Cu–S binding. Overall, our combined findings demonstrated that sulfur inclusion resulted in perturbation to the local Cu environment while the MOF structure remained largely intact.

Material properties like particle size and morphology are also critical for sulfur adsorption and charge conduction. CuBTC with average sizes of 0.16, 1.6 and 5.9 μm were synthesized (Fig. 1c) to study the impact of particle size on MOF–sulfur interaction. Although the bulk structure was identical for all sizes, differences in crystal orientation were apparent from powder X-ray diffraction (PXRD). Elemental analysis showed the total Cu content and the Cu to BTC ratio increased with decreasing particle size, which suggests the presence of truncated Cu paddlewheels and undercoordinated Cu sites on the particle surface.

To further probe the correlation between particle size and polysulfide retention, polysulfide dissolution was tested on open cells with 0.16 μm CuBTC@S, 5.9 μm CuBTC@S and S/C control cathodes, and the leaching amount was in the order of 0.16 μm < 5.9 μm < S/C. Electrochemical performance of CuBTC@S cathodes with different particle sizes was examined. The cathodes containing the smallest particle size, 0.16 μm CuBTC@S, outperformed in both maximum capacity and capacity retention (Fig. 1d and e), demonstrating its advantages in sulfur utilization and polysulfide uptake. These results illustrate small CuBTC particles, with their high density of undercoordinated surface Cu sites, provide enhanced polysulfide retention that led to enhanced battery performance. Overall, this work utilized a wide range of techniques to identify and characterize Cu–S interactions in CuBTC@S. The improved performance through manipulating particle sizes inspires rational design of nanomaterials with desirable surface morphology.

2.1.2. Polysulfide tethering groups. In addition to the use of Lewis acidic metal centers, another approach to mitigating the shuttle effect is to install covalent anchoring sites in the framework for polysulfides. Due to the synthetic versatility of MOFs, polysulfide anchor sites can be incorporated either on the organic linker or nodal structures.

2.1.2.1. Organic linker functionalization. Maleimide (Mi) groups have been previously used for fluorescent chemical sensing of thiols owing to their ability to react with thiols *via* a Michael Addition reaction.[33] UiO-66 is a well-studied Zr-based MOF composed of hexanuclear Zr clusters and 1,4-benzenedicarboxylic acid (H_2BDC) linkers. Utilizing UiO-66 as a platform, we have incorporated maleimide groups to the BDC linker (Mi-BDC) to study its tethering ability towards polysulfides (Fig. 2a).[34]

The molecular reactivity of maleimides with polysulfides was first examined by soaking the methyl ester analog (Mi-BDOMe) of Mi-BDC in polysulfide solution. Upon adding

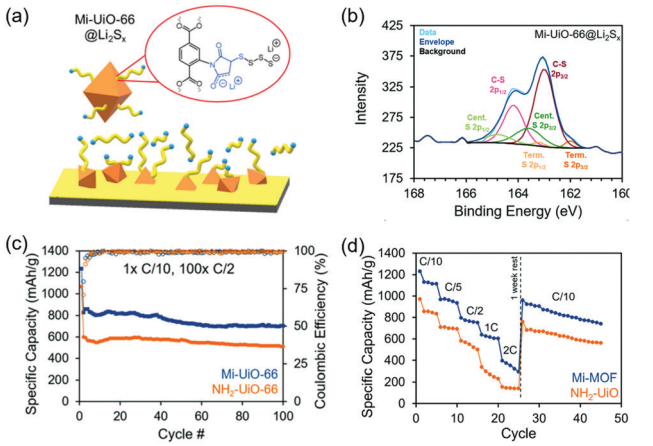

Fig. 2 (a) Depiction of Mi-UiO-66 upon the introduction of lithium polysulfides, (b) XPS spectra of the S 2p region of Mi-UiO-66@Li_2S_x, (c) specific capacity cycled at C/10 for 1 cycle and C/2 for 100 cycles, and (d) rate capability of Mi-UiO-66 (blue) and NH_2-UiO-66 (orange) cells. Reproduced from ref. 34 with permission from the Royal Society of Chemistry.

Mi-BDOMe, an immediate change of color from orange to deep red was observed. The visual color change as well as the red shift in UV-vis absorption spectra suggest the formation of maleimide enolate. The chemical reactivity between maleimide and polysulfides was further confirmed by fluorescence spectroscopy. With the addition of Mi-BDOMe, the peak emission wavelength shifted to the value matching with previously reported Mi-thiols.[33] Using *N*-phenyl maleimide (NPM) as a proxy for Mi-BDC, ^{1}H NMR spectra confirmed the disappearance of alkene protons and the appearance of features corresponding to the maleimide enolate upon exposure of Li_2S to NPM. Similarly, peaks corresponding to carbonyls and alkene shifted and a new feature at 52.3 ppm from C–S bond appeared in ^{13}C NMR spectra, confirming the Michael addition reaction between maleimide group and sulfides.

Following the molecular studies, Mi reactivity towards polysulfides in the solid state was also investigated, using a maleimide-functionalized UiO-66 (Mi-UiO-66) as a model. X-ray photoelectron spectroscopy (XPS) was performed on Mi-UiO-66 and pristine UiO-66 after soaking in Li_2S_8 solutions. Although Li_2S_x species were present in both MOFs, only Mi-UiO-66 exhibited features corresponding to the formation of C–S bonds (Fig. 2b). Such results support that Mi-UiO-66 is capable of chemically tethering polysulfide species, which is critical for avoiding polysulfide dissolution.

The polysulfide tethering ability of Mi-UiO-66 was further reflected in their cycling performance as a cathode additive. Relative to NH_2-UiO-66 controls, Mi-UiO-66 hosts showed enhanced capacity at various charge rates (C-rate, where 1C equals 1675 mA g^{-1}) and improved long-term capacity retention (Fig. 2c and d). The galvanostatic discharge curve of Mi-UiO-66 suggests a reduced cell polarization compared to NH_2-UiO-66, indicating the maleimide groups may also promote reaction kinetics for sulfur redox. With this effort, we incorporated an organic functional group into the linker to serve as a polysulfide

anchor and applied well-known molecular chemistry to Li–S battery cycling.

2.1.2.2 Open metal site functionalization. Other than tuning chemical properties by judicious selection of organic linkers, MOFs also permit post-synthetic engineering to further functionalize their nodal structures. To this end, Zr-based MOFs are ideal platforms since they possess versatile structure types, outstanding stability, and easily accessible open metal sites. By replacing the linkers or modulators bound to the metal node with polysulfide tethering groups, Zr-MOFs are expected to exhibit enhanced chemical interactions with polysulfides. Lithium phosphorus sulfides are well-known Li ion conductors and have been previously used as solid-state electrolytes.[35] It has also been previously shown that phosphorus sulfides can chemically interact with lithium polysulfides through S–S bond formation.[36] Leveraging these unique properties, our group installed Li_3PS_4 (LPS) at the Zr-MOF nodes (LPS-MOFs) to suppress polysulfide leaching in Li–S batteries (Fig. 3a).[37]

MOF-808 and UiO-66 were used as platforms for incorporating PS_4^{3-} moiety at the Zr node post-synthetically either through their intrinsic open sites (MOF-808) or introduced defect sites (UiO-66). Elemental analyses of LPS-MOFs exhibited increasing Li and P content with higher number of open sites, following the order of LPS-UiO-66 < LPS-MOF-808. The successful incorporation of PS_4^{3-} in MOFs was confirmed by NMR spectroscopy. Solution-state ^{31}P NMR spectroscopy of digested LPS-MOF samples showed a single peak at 89 ppm corresponding to PS_4^{3-} group. Notably, there were no peaks < 86 ppm from hydrolyzed thiophosphate species (PS_3O^{3-}, $PS_2O_2^{3-}$, PSO_3^{3-}), suggesting no P–S bond hydrolysis under the synthetic condition. This finding was further confirmed by air-free solid-state ^{31}P NMR spectroscopy of LPS-UiO-66. The spectra showed a phosphorus signal centered at 96.5 ppm, slightly shifted from the solid-state Li_3PS_4 at 87 ppm (Fig. 3b). With air exposure over 24 h scan time, a broad peak at ~52 ppm assigned to mixed P–S/P–O species began to grow. Combined, these results confirmed PS_4^{3-} moiety loaded in LPS-MOFs did not undergo hydrolysis and possessed a different local environment from crystalline Li_3PS_4.

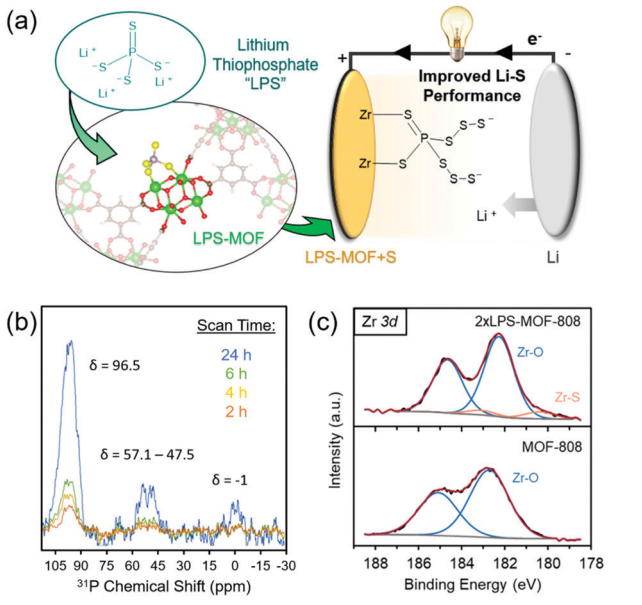

Fig. 3 (a) Illustration of thiophosphate-functionalized Zr-MOFs, (b) solid-state ^{31}P NMR spectra of LPS-UiO-66(50Benz), and (c) XPS of the Zr 3d region in MOF-808 and in 2×LPS-MOF-808. Adapted with permission from ref. 37. Copyright 2019 American Chemical Society.

We next determined the location of LPS functionalization in the framework using XPS, Raman spectroscopy, and pair distribution function (PDF). XPS was adopted to examine the chemical environment of Zr nodes and PS_4^{3-} moiety upon functionalization. A red shift of Zr $3d_{5/2}$ peaks observed in LPS-MOF compared to the parent framework suggested the thiophosphate was bound to the Zr node (Fig. 3c). Similarly, Raman spectra showed variations in the characteristic region for Zr–O bonds (200–400 cm^{-1}) for LPS-MOF, demonstrating PS_4^{3-} incorporation altered the vibrational modes of the nodal structure. PDF analysis provided additional structural evidence that PS_4^{3-} was bound to the Zr centers. Compared to pristine MOF-808, LPS-MOF-808 exhibited shifts at ~2.2 Å and ~3.5 Å, correlating to Zr–O and Zr–Zr, respectively. Taken together, the detailed chemical and structural analysis confirmed PS_4^{3-} was successfully incorporated in LPS-UiO-66 and LPS-MOF-808.

Electrochemical experiments were then performed on LPS-MOF sulfur composite cathodes to test their polysulfide tethering ability. Cyclic voltammetry (CV) of cells prepared with LPS-MOF+S (physically mixing) and LPS-MOF@S (melt diffusion) showed shifted reduction and oxidation potentials. LPS-MOF@S cells exhibited lower overpotentials for both reductive and oxidative events, suggesting LPS-MOF may electrochemically interact with polysulfides. For long-term cycling, the maximum capacity increases from 891 mA h g^{-1} in the parent UiO-66 cells to 1193 mA h g^{-1} in LPS-UiO-66 cells (Fig. 4a), confirming PS_4^{3-} can facilitate sulfur utilization. LPS-UiO-66 cells also showed improved capacity retention, delivering a specific capacity of 835 mA h g^{-1} after 100 cycles compared to only 560 mA h g^{-1} for UiO-66 cells. The attenuated capacity decay was attributed to the polysulfide tethering ability of LPS-MOFs.

The impact of LPS on cycling was further demonstrated by comparing MOFs with different LPS loading (n×LPS-MOF-808, n = 0.7, 1, and 2 stoichiometric equivalence). Compared to MOF-808 cells, LPS-MOF-808 cells showed maximum capacity increases of 70, 130, and 300 mA h g^{-1} for 0.7×, 1×, and 2×LPS-MOF-808, respectively (Fig. 4b). The fact that maximum capacity increased with higher PS_4^{3-} incorporation suggested further enhancement in cycling performance can be achieved with optimized loading. The polysulfide tethering ability of LPS-MOFs was also confirmed by the lower electrode surface resistance and less sulfur deposition on the Li anode after cycling. The structural importance of LPS-MOF in cycling was validated by LPS-ZrO_2 controls. Without the internal porosity, LPS-ZrO_2 cells failed within the first 100 cycles. This work illustrated the importance of polysulfide anchor group for enhancing electrochemical performance. This strategy can be extended to other porous matrix with desired structure and porosity.

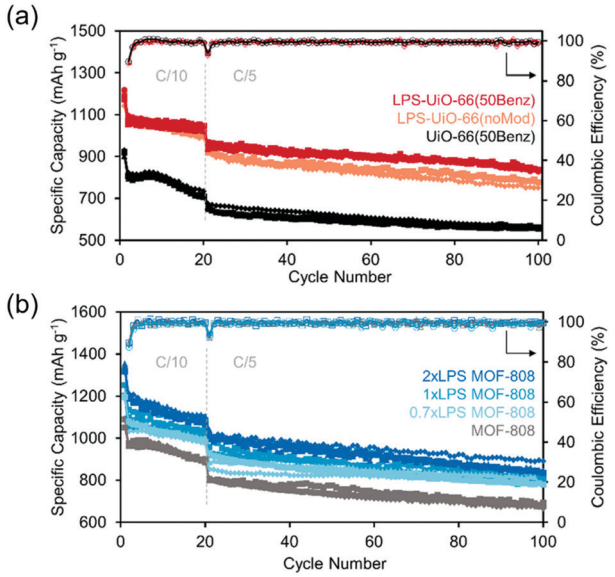

Fig. 4 Cycling performance for coin cells containing (a) UiO-66 and (b) MOF-808 series, showing improvements in the maximum capacity and capacity retention upon LPS incorporation. Adapted with permission from ref. 37. Copyright 2019 American Chemical Society.

Polysulfide tethering is critical for mitigating PS shuttle and enhancing electrochemical performance. Owing to the tunable nature of MOFs, MOF-polysulfide interactions can be promoted by judicious selection of metal nodes and organic linkers. Other than utilizing coordinatively unsaturated metal sites and linker functionalities, we installed PS anchor sites on nodal structures post-synthetically. These design strategies are promising for further exploration of porous networks in Li–S batteries.

2.2. Promoting charge transport in MOFs

Electronic and ionic transport are critical in electrochemical devices. Most MOFs exhibit low electronic conductivity due to the strong metal–oxygen bond at the node, limiting the performance of MOFs in Li–S batteries. The pore structure of the framework is also important for optimal ion mobility. Here, we demonstrate strategies to promote charge conduction in MOFs.

2.2.1. Node lithiation. Previous studies have shown enhanced specific capacity using Li-rich materials in S/C cathodes, since well-distributed Li ions can provide additional conduction pathways during cycling.[38] Combined with defect engineering, we extended this approach to MOF hosts by lithiating defect sites in Zr-MOF to boost local Li ion concentration (Fig. 5a).[39] UiO-66 was selected as the platform due to the ease of incorporating missing linker defects to the structure. Controlled amounts of trifluoroacetic acid (TFA) or benzoic acid (Benz) were used as modulators to introduce defects during synthesis. Through "HCl activation", the modulator linked to the Zr node was exchanged to terminal hydroxide and aquo ligands. The calculated number of missing linkers per Zr_6 node was 1.16, 1.57, and 1.82 for UiO-66(noMod), UiO-66(TFA), and UiO-66(Benz).

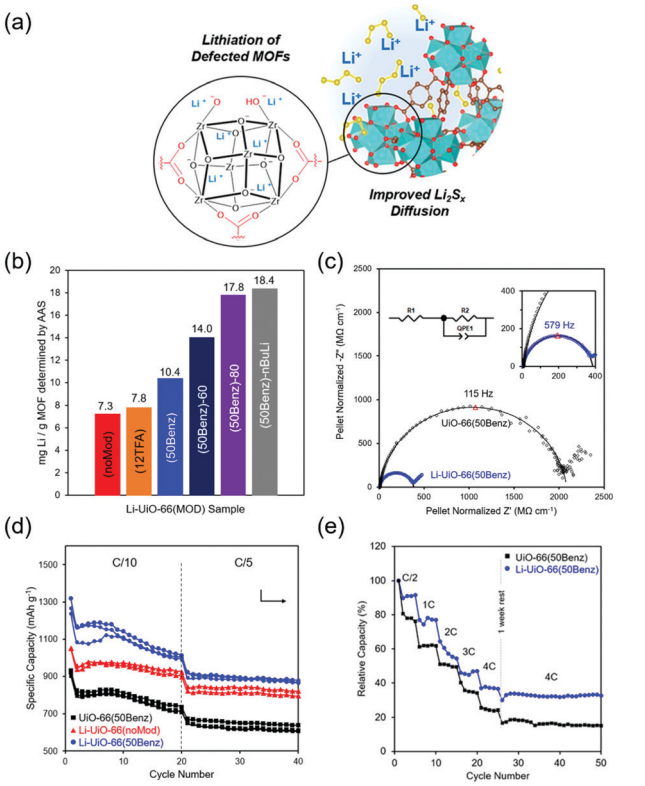

Fig. 5 (a) Scheme of lithiated defect sites in Zr-MOF, (b) Li incorporation measured by AAS for Li-UiO-66 series at various synthetic conditions, (c) Nyquist plots of UiO-66(50Benz) (black diamonds) and Li-UiO-66(50Benz) (blue circles), (d) discharge capacity as a function of cycle number for lithiated and non-lithiated MOF coin cells, and (e) rate capabilities for UiO-66(50Benz) (black square) and Li-UiO-66(50Benz) (blue circle). Adapted with permission from ref. 39. Copyright 2019 American Chemical Society.

The labile protons in defected UiO-66 were then replaced with Li ions under the basic conditions.

The structural integrity of lithiated MOFs was confirmed by PXRD and scanning electron microscopy (SEM). The Li content in Li-UiO-66 was determined by atomic absorption spectroscopy (AAS, Fig. 5b), showing concentration of defect sites was correlated with Li incorporation. Modifying synthetic conditions like raising the temperature or increasing basicity can also promote lithiation. Compared to Li-UiO-66(Benz), Li concentration can boost by 1.7× when elevating temperature to 80 °C, or 1.8× when changing the base to *n*-butyllithium. However, framework integrity and crystallinity were diminished under these harsher conditions. To further probe the impact of lithiation on Li ion conductivity, electrochemical impedance spectroscopy (EIS) was performed on pressed pellets formed from electrolyte-infiltrated MOF powders (Fig. 5c). The measured ionic conductivity at room temperature was 1.20×10^{-8} S cm^{-1} for Li-UiO-66(50Benz) and 1.98×10^{-9} S cm^{-1} for UiO-66(50Benz). Thus, the increase in ionic conductivity for Li-MOFs was attributed to Li incorporation.

Li–S cycling performance of MOF+S cathodes was further examined. The amount of defect sites within the framework did not significantly impact the sulfur utilization and capacity

retention; UiO-66(noMod), which contains no modulators, and UiO-66(50Benz) cathodes showed similar maximum discharge capacity and capacity retention. However, maximum capacity of cells containing lithiated MOFs was increased as a function of Li ion content. Li-UiO-66(50Benz) cathodes delivered a maximum capacity of 1272 mA h g^{-1} compared to 918 mA h g^{-1} of UiO-66(50Benz) (Fig. 5d). Interestingly, Li-UiO-66 additives synthesized under harsher conditions (*i.e.* elevated temperature, strong base) did not show enhanced capacity although they presented higher Li content. Such results suggest both Li ion incorporation and intact MOF structures are critical for sulfur utilization and ion transport.

EIS of cells post-cycling was analyzed to probe charge transport properties of lithiated and non-lithiated additives. Compared to UiO-66(50Benz) cells, Li-UiO-66(50Benz) cells showed reduced electrode surface resistance, charge transfer resistance, and Warburg impedance, indicating lithiated frameworks can mitigate polysulfide leaching and facilitate charge transfer and ion diffusion. Further evidence was provided by CVs of MOF+S cathodes. The peak current was fitted linearly *versus* the square root of scan rate. According to Randles–Sevcik equation, the slope of the plot is related to diffusion coefficients for electroactive species. Li-UiO-66(50Benz) cells showed larger slopes in both reduction steps, confirming enhanced ion transport with Li incorporation.

Finally, lithiated UiO-66 also showed improved performance at high C-rates. Compared to UiO-66(50Benz) cells, Li-UiO-66(50Benz) cells displayed improved capacity retention at all rates, especially above 2C (Fig. 5e). The improvement in rate capability validated that lithiated MOFs can facilitate charge transport, making them promising candidates for fast charge–discharge applications. This work demonstrated lithiated UiO-66 have positive impacts on sulfur utilization and ion diffusion, leading to enhanced capacity and retention at various C-rates. The lithiation strategy can be applied to other sulfur host materials with limited ionic conductivity.

2.2.2. Redox activity incorporation. Introducing redox activity to MOFs is another strategy for improving charge transfer. Redox active components can be installed on the organic linkers or incorporated at the open sites post-synthetically. Compared to commonly used redox-innocent linkers, anthraquinones (AQ) can undergo reversible redox reactions and store two electrons. Moreover, AQ linkers offer additional sites for lithium ions when reduced in lithium electrolyte, generating lithioquinones. Due to their advantages in storing and mobilizing electrons and lithium ions, AQ moiety has been previously utilized in cathodes for LIBs.[40]

In our work,[41] Zr oxide clusters were chosen as the metal nodes since they present great chemical stability and versatile functionality. Combining the redox feature of AQ linkers and porous structures of Zr-based framework, we developed Zr-AQ-MOFs as cathode additives to facilitate charge transport and enhance Li–S cycling (Fig. 6a). 2,6-Zr-AQ-MOF was synthesized under solvothermal procedure using 2,6-dicarboxy-9,10-anthraquinone as the linker. CV of 2,6-Zr-AQ-MOF showed a pair of redox peaks with a $E_{1/2}$ of 2.49 V *vs.* Li/Li^+ (Fig. 6b),

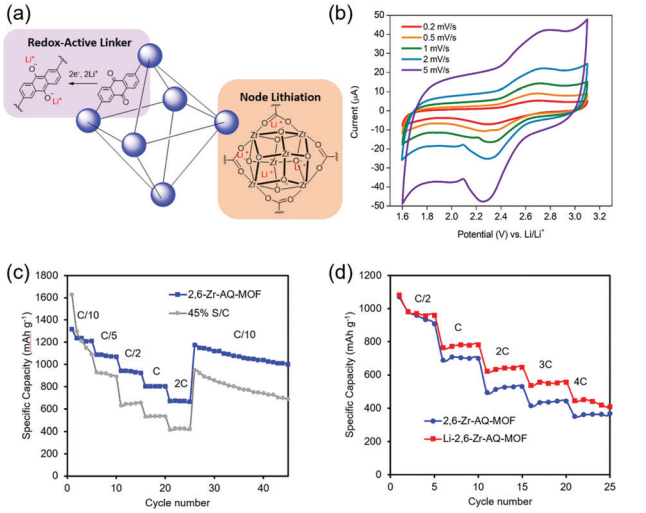

Fig. 6 (a) Scheme showing incorporation of AQ linkers in 2,6-Zr-AQ-MOF, (b) CV of 2,6-Zr-AQ-MOF at scan rates from 0.2 to 5 mV s^{-1}, (c) rate capabilities of 2,6-Zr-AQ-MOF and 45% S/C cells varied from C/10 to 2C, and (d) rate capabilities of 2,6-Zr-AQ-MOF and Li-2,6-Zr-AQ-MOF cells varied from C/2 to 4C. Adapted from ref. 41, Copyright 2019, with permission from Elsevier.

confirming its redox activity within the Li–S cycling voltage window.

To further illustrate the impact of AQ linker on performance, Zr-AQ-MOF+S cathodes were cycled at various C rates. 2,6-Zr-AQ-MOF cells delivered a capacity of 719 mA h g^{-1} after 300 cycles at 1C with little capacity decay, while S/C cells only exhibit 266 mA h g^{-1}. Importantly, 2,6-Zr-AQ-MOF cells showed much enhanced rate capability, delivering 667 mA h g^{-1} at 2C (Fig. 6c). Galvanostatic discharge profiles of 2,6-Zr-AQ-MOF cells exhibited flat plateaus and less sloping curves with higher capacity yield for both equilibrium regions at high C-rates compared to S/C cells. Thus, adopting AQ linker can facilitate redox electrokinetics and boost sulfur utilization.

To further improve the ionic conductivity of the framework, we extended the lithiation strategy to redox-active MOFs. Li content was quantified by AAS and acid–base titration, showing 0.398 wt% Li in Li-2,6-Zr-AQ-MOF and 1.19 Li atoms per Zr_6 cluster. As expected, pellet EIS of the lithiated framework showed enhanced ionic conductivity than pristine 2,6-Zr-AQ-MOF, being 4.8×10^{-7} S cm^{-1} and 2.4×10^{-8} S cm^{-1}, respectively. Interestingly, unlike Li-UiO-66(50Benz) cells, Li-2,6-Zr-AQ-MOF cells did not show large improvements over non-lithiated ones at low C-rates. However, the enhancements in specific capacity and capacity retention appeared at C-rates above C/2 (Fig. 6d) and long-term cycling at 4C. The different behaviors between Li-UiO-66 and Li-2,6-Zr-AQ-MOF further corroborate our theory that the AQ linker provided additional lithiation sites when reduced in electrolyte across the entire framework—further node lithiation did not significantly boost the sulfur utilization at low C-rates. Lithiated Zr nodes started to play a larger role at higher C-rates since high Li ion flux is critical for fast charge and discharge.

EIS of cells in the discharged state after cycling at 4C illustrated the impact of node lithiation on charge transfer

kinetics. Li-2,6-Zr-AQ-MOF cells showed lower electrolyte resistance, electrode surface resistance, and charge transfer resistance compared to 2,6-Zr-AQ-MOF cells. The smaller resistance values indicated Li-2,6-Zr-AQ-MOF enabled easier electrochemical accessibility to polysulfide species and faster redox kinetics.

2.2.3. Porosity tuning. Pore structure of MOF also plays an important role in charge transport. Porosity can affect charge transfer rate as it determines electron hopping distance and ion diffusion pathway simultaneously. Generally, larger pores permit high ion flux while decelerating electron migration. Previous studies on ferrocene incorporated MOFs showed ion diffusion is the rate-limiting step, and larger pores favor overall charge transfer efficiency.[42] To examine the combined effect of redox activity loading and porosity in MOFs on polysulfide redox, we installed anthraquinone-2-carboxylic acid linkers (AQ) to the open sites of Zr-MOFs (Fig. 7a).[43] Compared to utilizing AQ species as building units, open site functionalization allows greater tunability over loading amount and porosity.

Two types of Zr-MOFs, MOF-808 and NU-1000, with different pore sizes and number of open sites were selected as parent MOFs. AQ linkers were incorporated in MOFs post-synthetically by substituting monocarboxylate modulator bound to the Zr node under solvent-assisted ligand incorporation (SALI) procedure. Different loading content was achieved by tuning the amount of AQ linkers added in the SALI step. As determined by ^{1}H NMR spectroscopy of digested MOF-AQ samples, the ratio of AQ to Zr_6 node is 4, 3, and 1.5 for NU-1000-AQ, MOF-808-3×AQ, and MOF-808-1.5×AQ, respectively. The successful grafting of AQ was demonstrated in IR. Compared to the spectrum of AQ linker, the C=O stretch from carboxylic acid disappeared in MOF-AQs while C=O stretch from ketone groups remained and its intensity increased with higher AQ loading. Nitrogen adsorption isotherms were examined to probe the relationship between loading and porosity. As expected, BET surface area and pore volume reduced with increasing AQ incorporation, confirming higher AQ loading led to more blocked and crowded pore environments.

The incorporation of AQ was electrochemically demonstrated in CV with two pairs of peaks (Fig. 7b), corresponding to the two step one-electron redox reaction of grafted AQ linkers. Compared to the voltammogram of physical mixture of MOF and AQ linker, MOF-AQ exhibited anodic shift in reduction potential and smaller peak separations, demonstrating AQ moiety was more electrochemically active when infiltrated into MOF matrix. Slight anodic shifts in reduction potential were observed in NU-1000-AQ in contrast with MOF-808-3×AQ, suggesting larger channels made AQ species easier to be accessed and reduced. Additionally, the charge transfer in MOF-AQ solid matrix was diffusion-controlled since the peak currents fit linearly with square root of scan rate.

The critical role of AQ loading in facilitating charge transport and polysulfide redox was revealed in NU-1000-AQ. CVs of NU-1000+S and NU-1000-AQ+S cells were examined, both showing two reduction events and one broad oxidation feature. Normalized peak currents (based on sulfur mass) showed linear dependence on square root of scan rate for both stages (Fig. 7c). The larger slopes in NU-1000-AQ+S cell were related to a higher diffusion coefficient, illustrating AQ loading promoted ion diffusion. Consequently, MOF-AQ+S cells were cycled at various C-rates to examine their performance. For long-term cycling at C/2, NU-1000-AQ+S were able to deliver capacity of 693 mA h g^{-1} with high capacity retention after 100 cycles, while NU-1000+S exhibited 22% decrease in capacity and more capacity decay compared to NU-1000-AQ+S. More importantly, NU-1000-AQ+S presented outstanding rate capability and capacity recovery (Fig. 7d), enabling potential applications in fast charge–discharge devices. As evidenced in galvanostatic profiles and EIS, NU-1000-AQ+S showed smaller overpotential at high C rates and smaller resistance than NU-1000+S. Overall, the benefits of AQ loading on charge mobility and ion diffusion were illustrated.

Although AQ functionalization can facilitate polysulfide redox, it also took up significant pore space, potentially limiting high ion flux. To further illustrate that a delicate balance between loading and porosity should be achieved for optimized charge transfer efficiency, MOF-808 with different loadings were investigated. Although MOF-808-1.5×AQ had a lower AQ loading than MOF-808-3×AQ, the diffusion coefficient of MOF-808-1.5×AQ was higher, which suggested that free pore

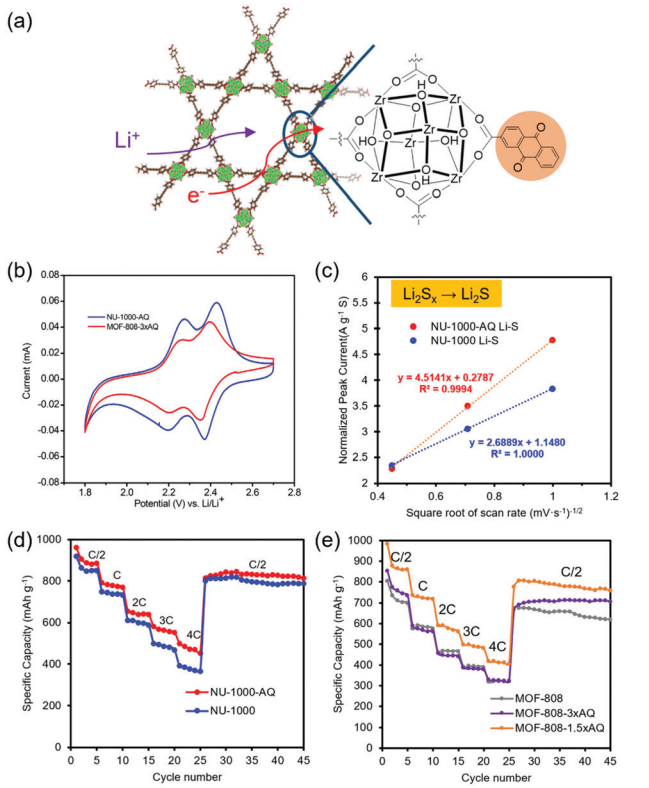

Fig. 7 (a) Illustration of charge transport in Zr-MOF-AQ, (b) CV of NU-1000-AQ and MOF-808-3×AQ, (c) sulfur mass-normalized peak current as a function of the square root of scan rate, and rate capabilities for (d) NU-1000 series and (e) MOF-808 series varied from C/2 to 4C. Adapted with permission from ref. 43. Copyright 2020 American Chemical Society.

volume was necessary for high flux. As expected, MOF-808-1.5×AQ+S cells showed highest capacity at all C-rates and good rate capability, while MOF-808-3×AQ+S only demonstrated slight to no improvements over MOF-808+S (Fig. 7e). In summary, the introduction of redox-active moiety to MOF matrix without severely lowering its porosity can enhance polysulfide redox and ion diffusion. Our effort to facilitate charge transport in MOFs through redox activity incorporation and porosity tuning motivates rational design of novel porous matrices to meet fast charge–discharge needs.

Charge transport is crucial in electrochemical devices, significantly affecting their energy output efficiency and overall performance. We employed several strategies to facilitate charge conduction in MOF matrices. By post-synthetically lithiating nodal structures, MOFs present improved Li ion conductivity and mobility. Through the incorporation of redox-active moieties either at linker or open metal sites, our functionalized MOFs demonstrate promoted charge transport and diffusion. We also discovered that porosity should be cautiously tuned for optimal charge transfer efficiency. These design criteria may also be transferrable to other porous solid-state materials.

3. Towards practical implementation of MOF-based Li–S batteries

Equipped with the design strategies discussed above, we focused on practical implementations of MOF-based cathodes. Adopting materials engineering and polysulfide tethering strategies, we constructed Li–S batteries with enhanced volumetric energy density and low-temperature tolerance.

3.1. High-density cathode through materials engineering

Despite the aforementioned advantages of adopting MOFs in Li–S energy storage devices, MOF-incorporated batteries may suffer from limited cycling performance due to their low electronic conductivity and low density. We have employed a materials engineering approach to address this issue by combining sulfur-impregnated MOF-808 with graphene/ethyl cellulose (GEC) additives to form a high-density nanocomposite electrode (MOF-808@S/GEC).[44] Herein, graphene was used to replace conventional carbon black in the cathode since graphene has higher conductivity and is expected to have better surface contact with the polyhedral MOF particles (Fig. 8a). Compared to our typical cathode slurry composition of physically mixed MOF, sulfur, super P, and polymer binder (MOF-808+S/SP), MOF-808@S/GEC permitted a more compact architecture, which is important for improving volumetric capacity.

Towards this end, sulfur was loaded into MOF-808 through melt diffusion process, and the sulfur loadings achieved 57 and 74% (in MOF-808@S) as determined by thermogravimetric analysis. Since the thiophosphate moiety can further enhance Li–S cyclability, LPS-MOF-808 (MOF-808 with node-bound lithium thiophosphate) was also loaded with sulfur, and the incorporation amount was 32 and 59% (in LPS-MOF-808@S).

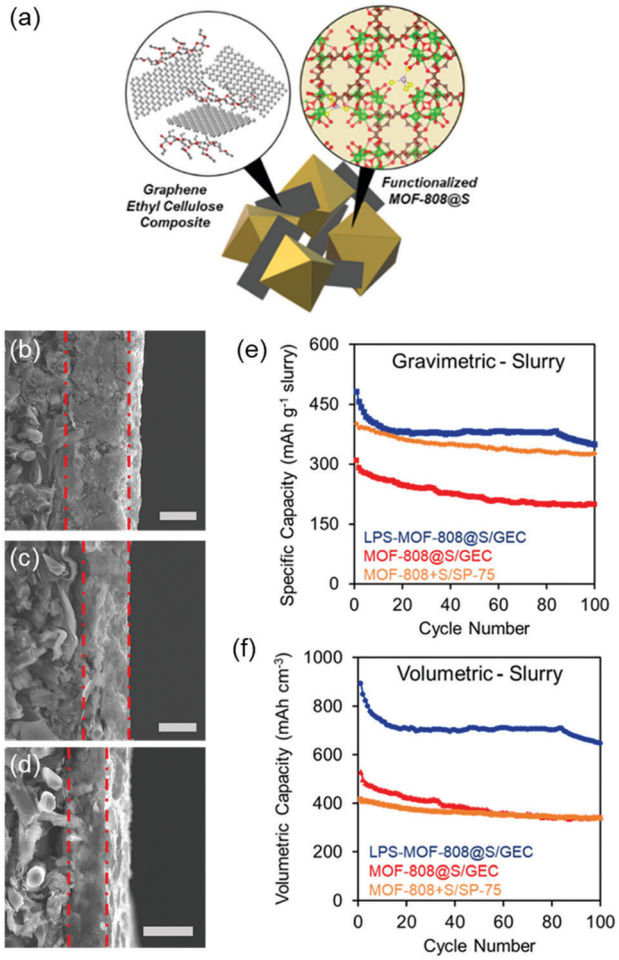

Fig. 8 (a) Depiction of MOF@S/GEC, cross-sectional profiles of carbon paper electrodes coated with (b) MOF-808+S/SP-75, (c) MOF-808@S/GEC, and (d) LPS-MOF-808@S/GEC slurries (scale bar is 20 μm), and (e) gravimetric and (f) volumetric capacity based on the slurry, highlighting the denser form factor of the MOF-808@S/GEC compared to MOF-808+S/SP-75 composite electrodes. Adapted with permission from ref. 44. Copyright 2020 American Chemical Society.

The synthesized GEC powder had 53% graphene and 47% ethyl cellulose by weight. SEM images of MOF-808@S/GEC demonstrated uniform distribution throughout the mixture and sulfur-loaded MOF particles were in close contact with graphene flakes.

XPS spectra for C 1s, S 2p and Zr 3d were examined for MOF-808@S/GEC, MOF-808@S/SP and MOF-808+S/SP samples to probe physical and chemical properties in different cathode slurries. In the C 1s spectra, MOF-808@S/GEC showed sp^2 peak at ~284 eV and sp^3 peak at ~285 eV, characteristic of graphene and ethyl cellulose, respectively. In S 2p and Zr 3d spectra, all samples exhibited similar features, while positive shifts in S $2p_{3/2}$ and Zr $3d_{5/2}$ peaks in MOF-808@S/GEC were observed. These positive shifts in S and Zr electron binding energies were attributed to electrostatic charge shifts, suggesting enhanced interfacial contact between MOF-808@S particles and GEC.

Subsequently, electrochemical experiments were performed on different slurries. SEM images of MOF-808@S/GEC and LPS-

MOF-808@S/GEC cathodes showed more compact coatings than MOF-808+S/SP (Fig. 8b–d). When cycled at C/2, MOF-808@S/GEC cells demonstrated enhanced gravimetric capacity than MOF-808@S/SP (Fig. 8e). Upon functionalization of MOF-808, LPS-MOF-808@S/GEC cells exhibited further improved sulfur utilization, delivering initial capacities of 858 ± 51 mA h g^{-1} with a capacity retention of 79.8%. The impact of slurry morphology on volumetric capacity was also investigated. LPS-MOF-808@S/GEC cells outperformed the others (Fig. 8f), illustrating the importance of materials engineering towards practical implementation. This strategy can be extended to other porous systems for advancing energy density in energy storage devices.

3.2. Polysulfide tethering for low temperature batteries

As we move towards widespread electrification, it is critical that energy storage devices can operate reliably and safely under various environments to meet commercial needs. However, at low temperatures, Li–S batteries suffer from poor cyclability due to sluggish charge transfer and ion diffusion. Specifically, the low solubility of Li_2S_x in electrolyte at reduced temperatures leads to incomplete discharge and polysulfide clustering. The aggregation of Li_2S_4 inhibits utilization of active materials, severely limiting energy output. A few studies have addressed this issue by optimizing electrolyte composition or modifying cathode materials to capture Li_2S_x at the electrode surface.[45,46] We have previously demonstrated that LPS functionalization in Zr-MOFs can effectively tether polysulfides and improve capacity.[37] We reasoned that the anionic thiophosphate group may also disrupt polysulfide clustering by electrostatically interacting with lithium polysulfides within the pores (Fig. 9a). Thus, we utilized LPS-functionalized UiO-66 and MOF-808 as cathode additives for low-temperature Li–S battery cycling.[47]

Adopting a slightly different electrolyte composition of 0.5 M lithium triflate and 0.5 M $LiNO_3$, we assembled coin cells that were cycled between −10 °C and 22 °C (RT) at the rate of C/10. As shown in Fig. 9b, cells containing MOF-LPS performed better than pristine MOF at all temperatures, with MOF-808-LPS and UiO-66-LPS delivering a capacity of nearly 810 and 530 mA h g^{-1}, respectively, after 20 cycles at −10 °C. Galvanostatic discharge profiles showed smaller cell polarization for MOF-LPS than the parent materials at low temperatures, which suggested LPS played a role in mitigating cell polarization. Additionally, different cycling mechanism at −10 °C was observed in MOF-LPS cells. In the discharge curves, other than the two characteristic plateaus (the upper one near 2.4 V *vs.* Li/Li^+ and the lower one near 2.1 V *vs.* Li/Li^+), a new plateau feature around 2.2 V *vs.* Li/Li^+ appeared (Fig. 9c). This additional feature indicated an extra equilibrium, likely attributed

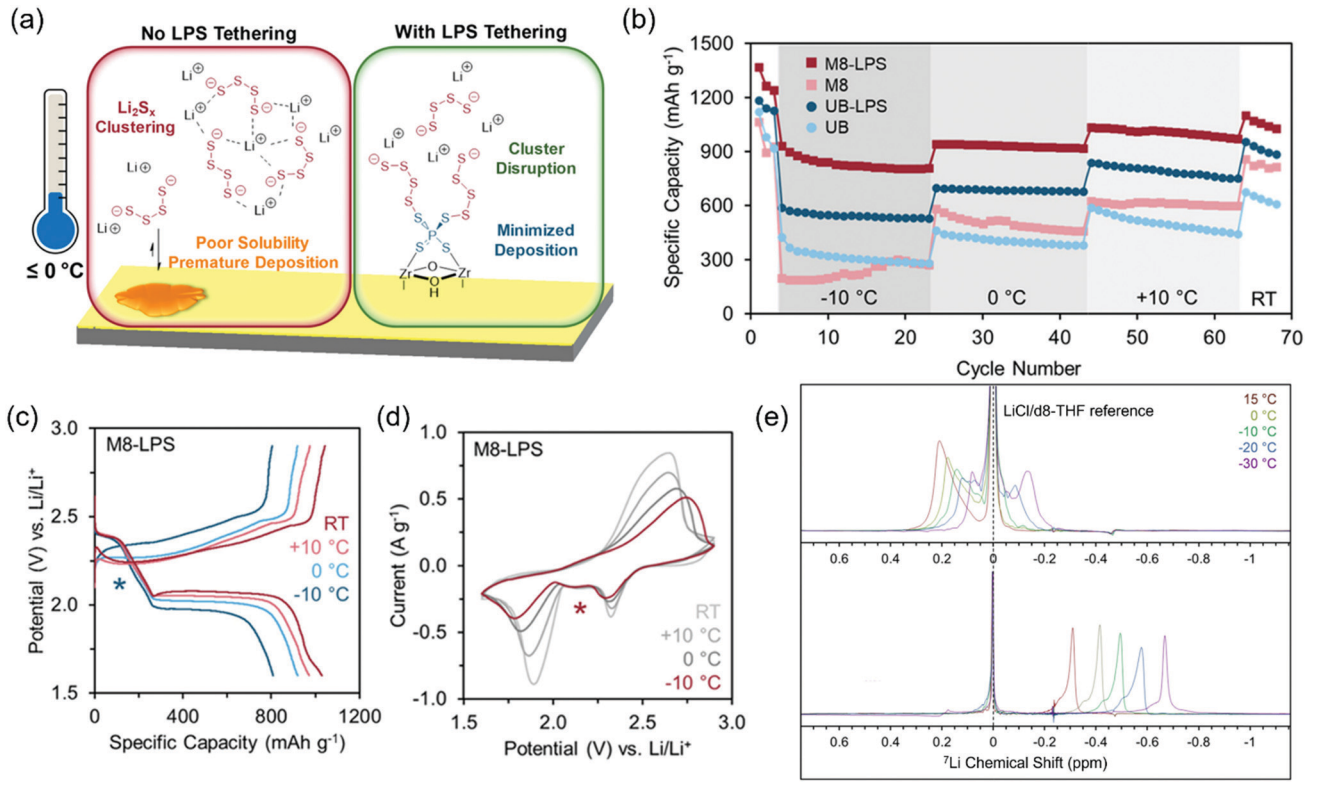

Fig. 9 (a) Scheme of chemical tethering *via* lithium thiophosphate improves electrochemical accessibility at low temperature, (b) discharge capacity of cells at various temperatures at C/10, (c) galvanostatic cycling curves of MOF-808-LPS at the final cycle for each temperature at C/10, (d) CVs for MOF-808-LPS at each temperature, and (e) variable-temperature ^7Li NMR spectra of 0.1 M Li_2S_4 (top) and 0.033 M P_2S_5 + 0.1 M Li_2S_4 (bottom) from 15 to −30 °C. Chemical shifts are calibrated to the LiCl/d-tetrahydrofuran (THF) reference peak (dotted line). Adapted with permission from ref. 47. Copyright 2021 American Chemical Society.

to the favorable chemical and electrostatic interaction between LPS and Li_2S_x at the electrode surface. The additional equilibrium may contribute to the sulfur utilization of MOF-LPS at mass transport limited conditions including high C-rate and low temperature. The different electrochemical mechanisms were further confirmed in variable temperature CV (Fig. 9d), showing an extra reductive feature. Galvanostatic intermittent titration technique (GITT) results demonstrated LPS incorporation led to larger and more stable diffusion coefficients at the lower plateau than parent MOFs.

The capability of LPS interrupting polysulfide clustering at low temperatures was illustrated by ^{7}Li NMR spectroscopy. ^{7}Li NMR spectra of Li_2S_4 solutions with and without thiophosphates in the temperature range of 15 to -30 °C were examined (Fig. 9e). In the absence of thiophosphate, the broad peak split into multiple peaks as temperature decreased, ascribed to various Li ion environments upon polysulfide clustering. In contrast, the peak profiles remained similar across the temperature range in the presence of thiophosphate, suggesting that thiophosphates can disrupt polysulfide clustering. This study demonstrated a promising approach for improving Li–S batteries performance at low temperature utilizing LPS-functionalized MOFs as cathode additives to chemically tethering polysulfides. This strategy can be extended to other sulfur-anchoring frameworks for batteries in extreme climates.

4. Conclusions

This feature article highlighted our design strategies for constructing multifunctional sulfur hosts for Li–S batteries. With judicious selection of organic linkers and post-synthetic modifications, MOFs can be tailored to facilitate polysulfide encapsulation, charge transport, and polysulfide redox. We also enhanced volumetric capacities and extended utilization of MOF matrices to battery cycling at low temperatures. Our synthetic and materials engineering approaches illustrate the potential of framework materials as cathode additives in Li–S batteries.

Future efforts should be focused on chemical strategies that increase the concentration of polysulfide anchors to prevent polysulfide dissolution. Charting the ion conduction pathways in MOFs is also necessary to promote charge mobility and increase the rate of charge and discharge. In addition, MOFs face major drawback of low electronic conductivity. Tailored electronic structures by tuning metal and linker components can enhance orbital overlap and favor charge delocalization "through-bond", resulting in a more conductive framework. The tunable pore structure of MOFs also provides a favorable environment for host–guest interactions, which can facilitate charge transfer "through-space" by introducing guest molecules.

Further optimization of MOF-based electrodes is required for practical implementation of Li–S batteries. For instance, high sulfur loading and low electrode porosity are necessary to obtain a final device with suitable gravimetric and volumetric energy densities and power densities. Thus, a fine balance between extending cycle life *via* the use of porous MOF additives and optimal energy densities must be achieved. Improving charge transport and installing redox active motifs that can store electrons in MOFs are a few ways to increase the sulfur loading and gravimetric energy density. Moreover, the infiltration of sulfur and other active components into the frameworks can decrease their overall porosity, while the use of alternative conductive substrates can lead to a volumetrically denser electrode.

Beyond their applications in energy storage devices, MOF-based systems can offer insights into structure–function relationships. Their versatile synthesis, high surface area, and remarkable crystallinity enable precise chemical and structural tuning that can be directly translated to macroscopic properties and redox behavior. Our fundamental understanding of these unique molecular frameworks can provide inspiration for developing advanced organic–inorganic hybrid materials for next-generation energy storage devices.

Conflicts of interest

There are no conflicts to declare.

Acknowledgements

We thank the Department of Chemistry and Johns Hopkins University for instrumentation support, graduate student support, and start-up funding. Our work has been supported by the National Science Foundation (Award #1945114). B. L. also thanks the William Hooper Grafflin Fellowship from the Department of Chemistry.

Notes and references

1 A. Manthiram, Y. Fu, S. H. Chung, C. Zu and Y. S. Su, *Chem. Rev.*, 2014, **114**, 11751–11787.
2 M. Wild, L. O'Neill, T. Zhang, R. Purkayastha, G. Minton, M. Marinescu and G. J. Offer, *Energy Environ. Sci.*, 2015, **8**, 3477–3494.
3 T. Li, X. Bai, U. Gulzar, Y. J. Bai, C. Capiglia, W. Deng, X. Zhou, Z. Liu, Z. Feng and R. Proietti Zaccaria, *Adv. Funct. Mater.*, 2019, **29**, 1901730.
4 M. Zhao, B. Q. Li, X. Q. Zhang, J. Q. Huang and Q. Zhang, *ACS Cent. Sci.*, 2020, **6**, 1095–1104.
5 C. Liang, N. J. Dudney and J. Y. Howe, *Chem. Mater.*, 2009, **21**, 4724–4730.
6 D. Li, F. Han, S. Wang, F. Cheng, Q. Sun and W. C. Li, *ACS Appl. Mater. Interfaces*, 2013, **5**, 2208–2213.
7 G. Zheng, Y. Yang, J. J. Cha, S. S. Hong and Y. Cui, *Nano Lett.*, 2011, **11**, 4462–4467.
8 C. Luo, S. Niu, G. Zhou, W. Lv, B. Li, F. Kang and Q. H. Yang, *Chem. Commun.*, 2016, **52**, 12143–12146.
9 S. Evers, T. Yim and L. F. Nazar, *J. Phys. Chem. C*, 2012, **116**, 19653–19658.
10 Z. W. Seh, W. Li, J. J. Cha, G. Zheng, Y. Yang, M. T. McDowell, P. C. Hsu and Y. Cui, *Nat. Commun.*, 2013, **4**, 1331.
11 L. Ni, G. Zhao, G. Yang, G. Niu, M. Chen and G. Diao, *ACS Appl. Mater. Interfaces*, 2017, **9**, 34793–34803.
12 Q. Zhang, Q. Huang, S.-M. Hao, S. Deng, Q. He, Z. Lin and Y. Yang, *Adv. Sci.*, 2021, 2103798.
13 S. Zeng, G. M. Arumugam, X. Liu, F. Guo, X. Li, H. Zhong and Y. Mai, *Chem. Commun.*, 2019, **55**, 12499–12502.

14 Y. Zhang, X. Zhang, J. Lyu, K. I. Otake, X. Wang, L. R. Redfern, C. D. Malliakas, Z. Li, T. Islamoglu, B. Wang and O. K. Farha, *J. Am. Chem. Soc.*, 2018, **140**, 11179–11183.
15 H. C. Zhou, J. R. Long and O. M. Yaghi, *Chem. Rev.*, 2012, **112**, 673–674.
16 A. E. Baumann, D. A. Burns, B. Liu and V. S. Thoi, *Commun. Chem.*, 2019, **2**, 86.
17 Y. Zhong, X. Xu, Y. Liu, W. Wang and Z. Shao, *Polyhedron*, 2018, **155**, 464–484.
18 Y. Zheng, S. Zheng, H. Xue and H. Pang, *J. Mater. Chem. A*, 2019, **7**, 3469–3491.
19 X. J. Hong, T. X. Tan, Y. K. Guo, X. Y. Tang, J. Y. Wang, W. Qin and Y. P. Cai, *Nanoscale*, 2018, **10**, 2774–2780.
20 Z. Wang, X. Li, Y. Cui, Y. Yang, H. Pan, Z. Wang, C. Wu, B. Chen and G. Qian, *Cryst. Growth Des.*, 2013, **13**, 5116–5120.
21 Y. Yang, Z. Wang, T. Jiang, C. Dong, Z. Mao, C. Lu, W. Sun and K. Sun, *J. Mater. Chem. A*, 2018, **6**, 13593–13598.
22 Y. Bai, Y. Dou, L. H. Xie, W. Rutledge, J. R. Li and H. C. Zhou, *Chem. Soc. Rev.*, 2016, **45**, 2327–2367.
23 N. Stock and S. Biswas, *Chem. Rev.*, 2011, **112**, 933–969.
24 S. Dissegna, K. Epp, W. R. Heinz, G. Kieslich and R. A. Fischer, *Adv. Mater.*, 2018, **30**, 1704501.
25 J. Zhou, R. Li, X. Fan, Y. Chen, R. Han, W. Li, J. Zheng, B. Wang and X. Li, *Energy Environ. Sci.*, 2014, **7**, 2715–2724.
26 H. Jiang, X.-C. Liu, Y. Wu, Y. Shu, X. Gong, F.-S. Ke and H. Deng, *Angew. Chem.*, 2018, **130**, 3980–3985.
27 J. H. Park, K. M. Choi, D. K. Lee, B. C. Moon, S. R. Shin, M. K. Song and J. K. Kang, *Sci. Rep.*, 2016, **6**, 25555.
28 X. F. Liu, X. Q. Guo, R. Wang, Q. C. Liu, Z. J. Li, S. Q. Zang and T. C. W. Mak, *J. Mater. Chem. A*, 2019, **7**, 2838–2844.
29 H. Park and D. J. Siegel, *Chem. Mater.*, 2017, **29**, 4932–4939.
30 Z. Wang, B. Wang, Y. Yang, Y. Cui, Z. Wang, B. Chen and G. Qian, *ACS Appl. Mater. Interfaces*, 2015, **7**, 20999–21004.
31 S. Bai, X. Liu, K. Zhu, S. Wu and H. Zhou, *Nat. Energy*, 2016, **1**, 16094.
32 A. E. Baumann, G. E. Aversa, A. Roy, M. L. Falk, N. M. Bedford and V. S. Thoi, *J. Mater. Chem. A*, 2018, **6**, 4811–4821.
33 Y. A. Li, C. W. Zhao, N. X. Zhu, Q. K. Liu, G. J. Chen, J. B. Liu, X. D. Zhao, J. P. Ma, S. Zhang and Y. Bin Dong, *Chem. Commun.*, 2015, **51**, 17672–17675.
34 D. A. Burns, A. Benavidez, J. L. Buckner and V. S. Thoi, *Mater. Adv.*, 2021, **2**, 2966–2970.
35 A. Miura, N. C. Rosero-Navarro, A. Sakuda, K. Tadanaga, N. H. H. Phuc, A. Matsuda, N. Machida, A. Hayashi and M. Tatsumisago, *Nat. Rev. Chem.*, 2019, **3**, 189–198.
36 Z. Lin, Z. Liu, W. Fu, N. J. Dudney and C. Liang, *Adv. Funct. Mater.*, 2013, **23**, 1064–1069.
37 A. E. Baumann, X. Han, M. M. Butala and V. S. Thoi, *J. Am. Chem. Soc.*, 2019, **141**, 17891–17899.
38 Z. Yang, R. Li and Z. Deng, *ACS Appl. Mater. Interfaces*, 2018, **10**, 13519–13527.
39 A. E. Baumann, D. A. Burns, J. C. Díaz and V. S. Thoi, *ACS Appl. Mater. Interfaces*, 2018, **11**, 2159–2167.
40 Z. Song, H. Zhan and Y. Zhou, *Chem. Commun.*, 2009, 448–450.
41 B. Liu, A. E. Baumann and V. S. Thoi, *Polyhedron*, 2019, **170**, 788–795.
42 P. J. Celis-Salazar, M. Cai, C. A. Cucinell, S. R. Ahrenholtz, C. C. Epley, P. M. Usov and A. J. Morris, *J. Am. Chem. Soc.*, 2019, **141**, 11947–11953.
43 B. Liu and V. S. Thoi, *Chem. Mater.*, 2020, **32**, 8450–8459.
44 A. E. Baumann, J. R. Downing, D. A. Burns, M. C. Hersam and V. S. Thoi, *ACS Appl. Mater. Interfaces*, 2020, **12**, 37173–37181.
45 A. Gupta, A. Bhargav, J. P. Jones, R. V. Bugga and A. Manthiram, *Chem. Mater.*, 2020, **32**, 2070–2077.
46 X. Wang, X. Zhao, C. Ma, Z. Yang, G. Chen, L. Wang, H. Yue, D. Zhang and Z. Sun, *J. Mater. Chem. A*, 2020, **8**, 1212–1220.
47 D. A. Burns, A. E. Baumann, K. J. Bennett, J. C. Díaz and V. S. Thoi, *ACS Appl. Mater. Interfaces*, 2021, **13**, 50862–50868.